The Journal of Experimental Biology 214, 1911-1921

doi:10.1242/jeb.052506

RESEARCH ARTICLE

A numerical study of the effects of bell pulsation dynamics and oral arms on the exchange currents generated by the upside-down jellyfish *Cassiopea xamachana*

Christina Hamlet[1], Arvind Santhanakrishnan[2] and Laura A. Miller[1,*]

[1]Department of Mathematics, University of North Carolina, CB 3250 Phillips Hall, Chapel Hill, NC 27599, USA and [2]Department of Biomedical Engineering, Georgia Institute of Technology, 315 Ferst Drive NW, Parker H. Petit Biotechnology Building, Atlanta, GA 30332-0363, USA

*Author for correspondence (lam9@email.unc.edu)

Accepted 6 February 2011

SUMMARY

Mathematical and experimental studies of the flows generated by jellyfish have focused primarily on mechanisms of swimming. More recent work has also considered the fluid dynamics of feeding from currents generated during swimming. Here we capitalize on the benthic lifestyle of the upside-down jellyfish (*Cassiopea xamachana*) to explore the fluid dynamics of feeding uncoupled from swimming. A two-dimensional mathematical model is developed to capture the fundamental characteristics of the motion of the unique concave bell shape. Given the prominence of the oral arms, this structure is included and modeled as a porous layer that perturbs the flow generated by bell contractions. The immersed boundary method is used to solve the fluid–structure interaction problem. Velocity fields obtained from live organisms using digital particle image velocimetry were used to validate the numerical simulations. Parameter sweeps were used to numerically explore the effects of changes in pulse dynamics and the properties of the oral arms independently. Numerical experiments allow the opportunity to examine physical effects and limits within and beyond the biologically relevant range to develop a better understanding of the system. The presence of the prominent oral arm structures in the field of flow increased the flux of new fluid from along the substrate to the bell. The numerical simulations also showed that the presence of pauses between bell expansion and the next contraction alters the flow of the fluid over the bell and through the oral arms.

Supplementary material available online at http://jeb.biologists.org/cgi/content/full/214/11/1911/DC1

Key words: jellyfish, biomechanics, computational fluid dynamics, feeding current, mathematical model.

INTRODUCTION

The genus *Cassiopea* of the phylum Cnidaria contains jellyfish found throughout the world in shallow, often stagnant marine environments (Templeman and Kingsford, 2010; Welsh et al., 2009). Although capable of locomotion, these organisms spend the majority of their time on the seafloor with the aboral portion of their bell resting against the substrate. Cnidarians such as *Cassiopea*, which harbor symbiotic zooxanthellae, have been shown to be sources of oxygen and removers of nitrogen and other inorganic nutrients, especially in lighted areas (Welsh et al., 2009; West et al., 2009). Recent studies have shown that members of *Cassiopea* themselves may be used as indicators of ecosystem health and to detect the presence of certain pollutants due to the incorporation of trace elements during particle transfer (Templeman and Kingsford, 2010). The sedentary lifestyle of *Cassiopea* spp. makes them more dependent than other foraging medusae on the nutrient exchange in their immediate surrounding environment. These organisms typically live in shallow inshore bays, near seagrass beds and in mangrove swamps that are characterized by low flow velocities. For example, flow velocities near and within seagrass beds can be on the order of $1\,cm\,s^{-1}$ or lower (Bartleson, 2004). Although there are little data on flow rates through mangrove swamps, maximum velocities may reach up to $0.7\,m\,s^{-1}$, but flow rates within densely packed swamps near the seafloor are likely significantly lower (Wolanski, 1992). Given their sedentary lifestyle and the slow surrounding flow rates, *Cassiopea* spp. rely on bell pulsations to generate flows necessary for particle exchange including food capture, oxygen exchange, temperature regulation, incorporation of zooxanthallae, waste elimination and gamete distribution (Arai, 1996; Welsh et al., 2009).

The mechanism of the bell contraction and expansion that generates flow seems relatively simple, but is the result of a coordinated system of muscles and viscoelastic tissue. Contractions are driven by coronal muscles and pinnate radial muscles (Arai, 1996). These muscles are surrounded by an organic matrix called the mesoglea that stores elastic energy generated during contraction. As the bell relaxes, the energy is released from the bell, resulting in passive expansion. Like other members of the order Rhizostomae, *Cassiopea* spp. lack tentacles and the four oral lobes are fused over the central mouth, forming a canal-like system of tiny suctioning mouth-like structures opening along eight branching oral arms (Fig. 1) (Brusca and Brusca, 2003; Hyman, 1940). Unlike many other medusae that serve as models for locomotion studies, the oral arm structure comprises a large part of the overall body of the organism (Arai, 1996; Dabiri et al., 2010; Daniel, 1985; Demont and Gosline, 1988; Lipinski and Mohseni, 2009). Sampling and capture of zooplankton prey occurs when water is driven over and across the oral arms.

Jellyfish have been the subject of vigorous biomechanical and fluid dynamic research aimed at understanding the nature of unsteady propulsion (Dabiri, 2005; Dabiri et al., 2007; Daniel, 1985;

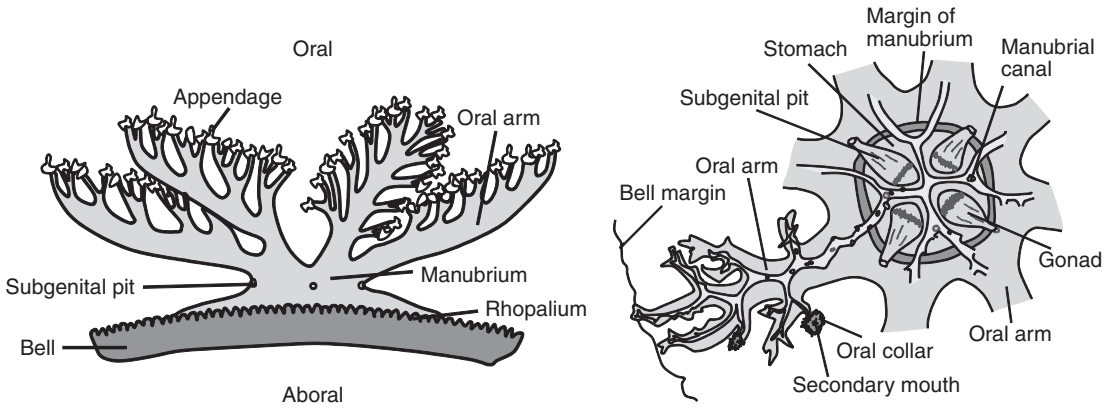

Fig. 1. The main structures of *Cassiopea xamchana* [drawn after Hyman (Hyman, 1940)]. The most salient features for the study are the bell and the oral arm appendages.

Daniel, 1995; Demont and Gosline, 1988; Lipinski and Mohseni, 2009; Rudolf, 2007; Sahin et al., 2009). Demont and Gosline (Demont and Gosline, 1988) and Daniel (Daniel, 1985) showed that the bell is driven at its resonant frequency, which increases the efficiency of this form of unsteady locomotion. More recent studies have used digital particle image velocimetry (dPIV) and Lagrangian coherent structures to characterize the vortex shedding, mixing and particle capture associated with jellyfish locomotion (Dabiri, 2008; Dabiri et al., 2010; Peng and Dabiri, 2008a; Peng and Dabiri, 2008b; Peng and Dabiri, 2009; Sahin et al., 2009). Rudolf used immersed boundary methods to develop animations of swimming jellyfish (Rudolf, 2007). Lipinski and Mohseni showed through computational studies that the vortex patterns generated by the bell motion of *Aequora victoria*, an oblate medusa, draws fluid through the organism's tentacles, enhancing its chances for nutrient sampling, whereas the vortex shedding by the prolate *Sarsia tubulosa* ejects fluid far from the bell, presenting little opportunity for localized foraging (Lipinski and Mohseni, 2009). Lipinski and Mohseni conjecture that the difference in the prominence and positioning of tentacles and oral arms in each organism is influenced by the swimming mechanisms employed to enhance foraging success.

The present study capitalizes upon the unique properties of *Cassiopea* in order to examine the pulse-driven flow of water over the oral arms uncoupled from swimming. Because feeding and other types of particle exchange rely on fluid flow around the prominent oral arms, it is important to include the oral arms in any sort of examination of flow around the bell of *Cassiopea*. A mathematical model of an idealized *Cassiopea* bell and oral arms is constructed and used in immersed boundary simulations to examine the effects of bell motion and secondary structures on the bulk flow. This model differs from that of previous studies in that it takes into account the oral arms as a separate and prominent structure of the organism.

This computational study allows for the exploration of how the bulk flows generated by *Cassiopea* vary with scale, pulse frequency and porosity of the oral arms within and beyond the biological range. For instance, the flow structures in the absence of the oral arms can be captured without altering the pulsing mechanism through invasive procedures necessary when using real organisms. This is useful for understanding how the presence of the oral arms as an obstruction to the flow can alter the bulk flow and affect rates of particle transfer between an organism and its surroundings. Exploration of a wide parameter space can be used to test the physical limits of transport mechanisms and to identify cooperative or complementary feeding and exchange mechanisms. In this study, the contraction kinematics, the presence and porosity of the oral arms and the Reynolds number are varied across and beyond the range of biologically relevant parameters. The effect on flow across the oral arms and across the bell is examined by calculating net flow rates going towards and away from the bell.

MATERIALS AND METHODS

Measurements

Specimens of *Cassiopea xamachana* Bigelow 1892 were obtained from Carolina Biological Company (Burlington, NC, USA) and maintained in the laboratory in standard 29 gallon aquaria. Video footage of the organisms was obtained using a Panasonic Palmcorder (model no. PV-GS300, 29.97 frames s^{-1}; Secaucus, NJ, USA). The timing of the pulse cycle was analyzed over 410 s of footage using iMovie software (Apple, Inc., Cupertino, CA, USA) to obtain a realistic cycle pattern. The contraction of the bell was defined as the time during which the sides of the bell move towards the central axis. The first pause is defined as the time during which the muscles cease to contract and the bell appears motionless before beginning its expansion. The expansion is defined as the motion of the bell out from the central axis of the organism. Finally, the second pause is defined as the time that the bell appears motionless before the next contraction begins. This pattern of motion was used as an input for the mathematical model of the organism.

Construction of the model

An approximate model of the primary bell shape was developed for use as an input into the simulations. Extending previous models (Daniel, 1985; Lipinski and Mohseni, 2009; Wilson et al., 2009) that describe jellyfish using hemiellipsoids or functions fit to digitized bell shapes, a simple mathematical model was constructed herein that captures the fundamental features of the organism. The models presented here also include a representation of the oral arms as a separate, prominent structure. This addition represents a novel feature in this paper as previous studies have typically ignored the effect of oral arms. In such work this simplification is permissible because the focus organisms are characterized by reduced oral arm structures. However, the oral arms are an integral part of *C. xamachana* and must be included here.

A simplified two-dimensional model of the bell of *C. xamachana* was constructed to make multiple parameter sweeps feasible. The aboral region resting against the substrate is defined as a line of length L. The choice of a line is justified by the fact that there is no flow under the aboral side of the jellyfish bell and this area of

the jellyfish is often lightly suctioned or adhered to the seafloor (Arai, 1996). This adhered portion only slightly dilates during pulsation so this section is assumed to be of constant length throughout the motion. Two reference configurations were defined as a completely contracted state and a completely expanded state. The curve of each of these configurations is defined by:

$$(x,y)(\theta,t)=\left[\frac{L}{A(t)}\right]\left\{\cos\left[\frac{\pi}{B(t)}+2\pi\theta\right],C(t)\sin\left[\frac{\pi}{B(t)}+2\pi\theta\right]\right\}, \quad (1)$$

where $A(t)$, $B(t)$ and $C(t)$ change in time in order to contract and expand the bell margins and θ is equal to the angle between the major axis of the ellipse and the line drawn from the center of the ellipse to the corresponding point on the boundary. Let t_1^i be the time when the ith bell contraction begins, t_2^i denote the time when contraction ends, t_3^i be the time when the subsequent bell expansion begins and t_4^i equal the time when bell expansion ends. The length of the first pause between the end of the bell contraction and the next expansion is t_3^i–t_2^i, and the length of the second pause between the bell expansion and the next contraction is t_1^{i+1}–t_4^i. The equations for $A(t)$, $B(t)$ and $C(t)$ are then given as:

$$A(t)=16-12\frac{t-t_1^i}{t_2^i-t_1^i},\ B(t)=2-3\frac{t-t_1^i}{t_2^i-t_1^i},$$

$$C(t)=1+\frac{t-t_1^i}{t_2^i-t_1^i},\ t_1^i\le t<t_2^i \quad (2)$$

$$A(t)=4,\ B(t)=-1,\ C(t)=2,\ t_2^i\le t<t_3^i \quad (3)$$

$$A(t)=4+12\frac{t-t_3^i}{t_4^i-t_3^i},\ B(t)=-1+3\frac{t-t_3^i}{t_4^i-t_3^i},$$

$$C(t)=2-\frac{t-t_3^i}{t_4^i-t_3^i},\ t_3^i\le t<t_4^i \quad (4)$$

$$A(t)=16,\ B(t)=2,\ C(t)=1,\ t_4^i\le t<t_1^{i+1}\ . \quad (5)$$

$A(t)$, $B(t)$ and $C(t)$ were chosen such that the conformations have relatively simple geometries and so that the distance traveled by the tip of the bell margin during each pulse is within the range relevant to the organism. To determine intermediate conformations between fully expanded and fully contracted configurations, the equations were derived such that the position is linearly interpolated using the calculated motion times from the video footage. These times were set equal to 0.6 s for contraction (t_2^i–t_1^i), 0.13 s for the first pause (t_3^i–t_2^i), 0.7 s for expansion (t_4^i–t_3^i) and 2.0 s for the second pause (t_1^{i+1}–t_1^i). The standard deviations of each of these measurements were 0.17, 0.06, 0.13 and 1.30, respectively, with a sample size of 150. These parameters were considered to be biologically reasonable but in no way comprised a comprehensive description of the motion of the organism.

The Reynolds number (Re) is the dimensionless scaling parameter that reflects the ratio of the effect of inertial forces in a flow to the effect of viscous forces. For $Re\ll1$, viscous forces are dominant in the system. For $Re\gg1$, inertial forces are significant whereas viscous forces are often negligible. The Re is defined using the equation $Re=\rho LU/\mu$, where ρ is the density of the fluid, L is the length of the aboral region of the bell, U is the mean velocity of the tip of the bell during contraction and μ is the viscosity of the fluid. The Re for adult *C. xamachana* is generally in the hundreds. The majority of the numerical simulations performed were conducted at $Re\approx450$, which is within the biological range of the organism. Some simulations were also performed at $Re\approx45$, which is at the scale of the juvenile ephyra that do not sit on the ocean floor to feed. This Re choice was included to examine the size limits of pulse-driven fluid transport.

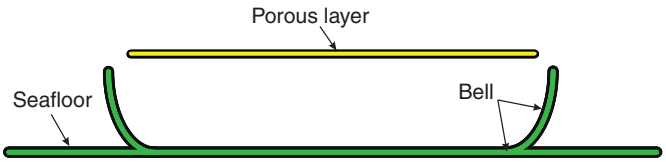

Fig. 2. The general setup of the jellyfish model. The porous layer is shown in yellow. The seafloor and main part of the jellyfish bell are shown in green and black.

The effects of pauses between pulses (the so-defined second pause) on the resulting fluid motion were considered. From the analysis of video data, the organism transitions between two basic states of pausing. The representative organism displayed a second pause between 1.0 and 3.5 s, whereas the remainder of the time a slight delay between 0.13 and 0.4 s was observed. It is important to note that there is significant variation in the pulsing frequencies of *Cassiopea* and other jellyfish (Colin and Costello, 2003), and the values used here were selected from a representative organism. In the numerical simulations, the pause time was varied to test the effect of the length of the pause on the bulk flow around the bell. It is important to note that the computational model allows one parameter to be varied in a controlled and specified manner, and this is a significant advantage of numerical simulations.

To examine the effect of the oral arms on the bulk flow, a simple model of the oral arms was constructed as a porous line placed just above the top of the bell. A schematic of the bell and oral arm model is shown in Fig. 2. This model is used to provide an obstruction to the flow while still allowing some fluid transport through the layer. In reality, the flow through the elaborate oral arms represents a challenging multiscale problem. It is currently not feasible to accurately capture both the large-scale flow patterns generated by the bell while also resolving the fine details of the flow through the branches of the oral arms. Some of the challenges of even relatively simple fluid–structure interaction problems are discussed in Beale and Layton (Beale and Layton, 2009) and Hou and Shi (Hou and Shi, 2008). The model presented here represents a first step in understanding the effect of the oral arms on the bulk flow generated by the jellyfish. The porosity of the oral arm model allows water to flow through this layer, and this is one of the most obvious features that should be retained in this study on fluid transport. For a first approximation of porosity, a homogeneous material is assumed. The computational methods used to describe the porous layer are given below.

Immersed boundary method

The immersed boundary (IB) method was originally developed by Peskin in the 1970s to simulate blood flow through the human heart (Peskin, 1977; Peskin, 2002). Since its construction, the IB method and others inspired by it have gained a great deal of popularity as computational solutions to fluid–structure interaction problems at low to moderate Re (Mittal and Iaccarino, 2005). The IB method has been used to simulate biological systems and materials including, but not limited to, swimming organisms, insect flight, platelet aggregation, cell motility, biofilms, foams, parachuting and paper pulp fibers (Dillon et al., 2007; Dillon et al., 2006; Fauci and Peskin, 1988; Fogelson and Guy, 2008; Kim et al., 2010; Kim and Peskin, 2006; Miller and Peskin, 2009; Stockie, 2009; Stockie and Green, 1998; Teran et al., 2010; Teran and Peskin, 2009; West et al., 2009). For details on the derivation and construction of the IB method see Peskin (Peskin, 2002).

The idea of the IB method is based on the definition of the fluid and the structure in separate frames. A viscous, incompressible fluid is discretized at node points on a fixed Cartesian grid (the Eulerian frame) with appropriate boundary conditions. The structure is defined as an immersed boundary and is discretized in a moving Lagrangian framework with reference to the Cartesian grid, but independent of the node points. Defined in this way, the discretization of the fluid grid can be relatively coarse while still allowing for complex geometries of the structure. Because the fluid grid does not need to be redefined as the boundary moves through it, computational times for simulations are greatly reduced.

The governing equations for the fluid are the two-dimensional Navier–Stokes equations for a viscous, incompressible fluid given by:

$$\rho\left[\frac{\partial \mathbf{u}(\mathbf{x},t)}{\partial t} + \mathbf{u}(\mathbf{x},t)\bullet\nabla\mathbf{u}(\mathbf{x},t)\right] = -\nabla p(\mathbf{x},t) + \mu\nabla^2\mathbf{u}(\mathbf{x},t) + \mathbf{f}(\mathbf{x},t) \quad (6)$$

$$\nabla\bullet\mathbf{u}(\mathbf{x},t) = 0\ , \quad (7)$$

where ρ is the fluid density, $p(\mathbf{x},t)$ is the fluid pressure, μ is the dynamic viscosity of the fluid, $\mathbf{u}(\mathbf{x},t)$ is the fluid velocity, $\mathbf{f}(\mathbf{x},t)$ is the force per unit area acting on the fluid, $\mathbf{x}$ is the position of the fluid node point and t is the time. Note that Eqn 6 is the momentum equation and Eqn 7 is the incompressibility condition.

To approximate the force that the boundary applies to the fluid, moving tether points may be employed. This method is commonly used when a desired configuration or preferred mode of active force must be enforced (Fauci and Fogelson, 1993; Fauci and McDonald, 1995; Watton et al., 2007). Here the preferred configuration $\mathbf{Y}(s,t)$ will be defined by the position of the constructed mathematical model described by Eqns 1–5 of the bell at time t. The boundary is tethered to the preferred configuration by a set of elastic springs. The stiffness of the springs, k, is chosen such that as the preferred boundary is stepped through time, a force required to move the actual boundary close to the preferred position is generated. Thus the structural equation in the Lagrangian framework is the simple Hookean relationship assuming zero rest-length springs given by:

$$\mathbf{F}[\mathbf{X}(s,t),t] = k[\mathbf{X}(s,t) - \mathbf{Y}(s,t)]\ . \quad (8)$$

This function is a force density defined along the immersed boundary.

The equations defined in the Lagrangian framework (Eqn 8) and in the Eulerian framework (Eqns 6, 7) are coupled through the following fluid–structure interaction equations:

$$\mathbf{f}(\mathbf{x},t) = \int\mathbf{F}[\mathbf{X}(s,t),t]\delta[\mathbf{x} - \mathbf{X}(s,t)]\mathrm{d}s\ , \quad (9)$$

$$\frac{\partial \mathbf{X}}{\partial t} = \mathbf{U}\left[\mathbf{X}(s,t)\right] = \int\mathbf{u}(\mathbf{x},t)\delta\left[\mathbf{x} - \mathbf{X}(s,t)\right]d\mathbf{x}\ , \quad (10)$$

where $\mathbf{F}(s,t)$ is the force per unit length acting on the fluid, $\mathbf{X}(s,t)$ gives the Cartesian coordinates of the boundary, s is the arc length along the boundary and $\mathbf{U}(s,t)$ is the local fluid velocity at the boundary points. Eqn 9 communicates the force exerted by the boundary on the fluid grid using a smoothed two-dimensional Dirac delta function $\delta(\mathbf{x})$. Once the Navier–Stokes equations have updated the fluid information for the time step, Eqn 10 is used to interpolate the local fluid velocity at each boundary point and move the boundary at the calculated velocity. This enforces the no-slip condition associated with a viscous fluid. The exact numerical algorithm used in this paper is described in detail in Peskin and McQueen (Peskin and McQueen, 1996) with the exception of the discretization of the δ-function. The choice of δ-function used here is detailed in Peskin and Printz (Peskin and Printz, 1993) and given by the following equations:

$$\delta_{\Delta x} = \Delta x^{-2}\phi\left(\frac{x}{\Delta x}\right)\phi\left(\frac{y}{\Delta x}\right) \quad (11)$$

$$\phi(r) = \begin{cases}\frac{1}{4}\left[1+\cos\left(\frac{\pi r}{2}\right)\right] & \text{if } |r| \le 2\\ 0 & \text{otherwise}\end{cases} \quad (12)$$

where Δx is the spatial step size in both the x- and y-directions, ϕ is a function used in the construction of the delta function, r is the non-dimensional distance from the Eulerian node point and $\delta_{\Delta x}$ denotes the discretized version of the δ-function.

To summarize, the basic steps of the method are as follows: (1) a force is imposed on the immersed boundary; (2) the force is translated on the fluid grid using a smoothed approximation to the Dirac function; (3) the fluid equations are solved using an appropriate numerical solver; (4) the boundary is moved at the local fluid velocity, which is found through interpolation using the smoothed delta function to enforce the no-slip condition; and (5) the simulation advances to the next time step.

The complex structure of the eight oral arms is modeled as a porous layer using the method derived by Kim and Peskin (Kim and Peskin, 2006) and Stockie (Stockie, 2009). Permeability is incorporated into the IB method using Darcy's law, which states that the relative velocity of a fluid through a porous medium is proportional to the pressure difference across the boundary:

$$q = \frac{-\kappa}{\mu}\left[P\right]\ , \quad (13)$$

where q is the Darcy flux (discharge per unit area), κ is the permeability of the layer and $[P]$ is the pressure jump across the layer.

Table 1. Default values of all parameters in the simulations unless otherwise noted

Parameter	Symbol/equation	Units	Value
Density	ρ	kg m^{-3}	998
Body length	L	m	0.0508
Porosity coefficient	λ	m^2 (N s)$^{-1}$	0.00000072
Total cycle period	$t_1^{i+1}-t_1^i$	s	3.43
Cycle period	$t_4^i-t_1^i$	s	1.43
Duty cycle	$(t_2^i-t_1^i)/(t_4^i-t_1^i)$	–	0.4196
1st pause	$t_3^i-t_2^i$	s	0.13
2nd pause	$t_1^{i+1}-t_4^i$	s	2.0
Total period	–	s	3.43

Table 2. Values of all numerical parameters unless otherwise noted

Numerical parameter	Symbol	Units	Value
Time step	dt	s	0.00006096
Spatial step Cartesian grid	Δx	m	0.000396875
Spatial step Lagrangian grid	Δs	m	0.000198438
Domain size	–	m	0.2032
Stiffness coefficient, boundaries	k	N m^{-1}	13987028
Stiffness coefficient, arms	k_{arm}	N m^{-1}	139870.28
Fluid grid size	–	–	512x512

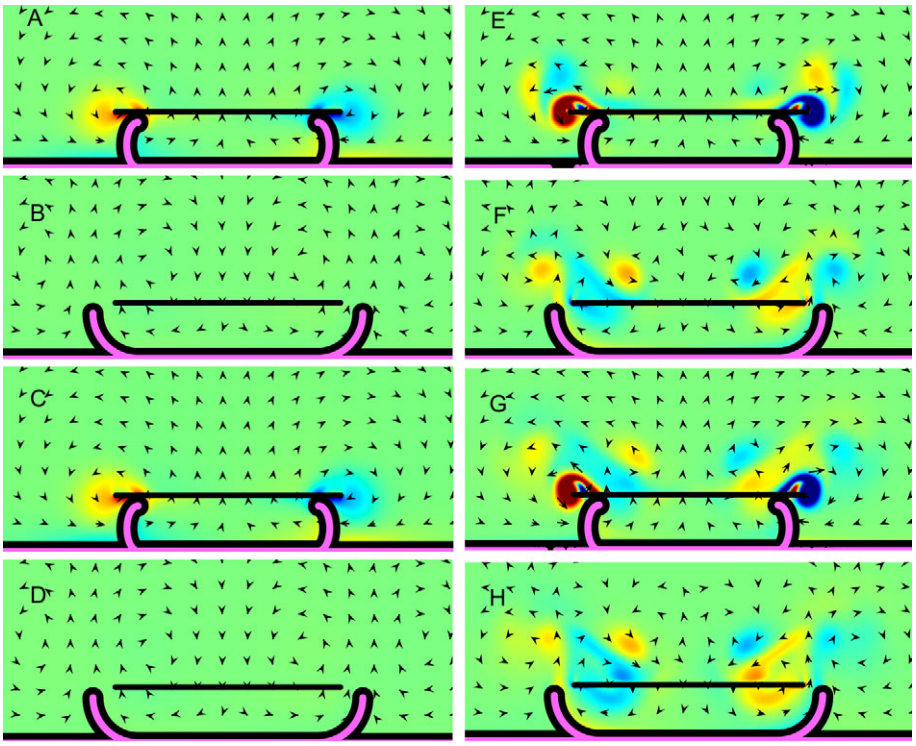

Fig. 3. Vorticity plots from numerical simulations with overlaid velocity vector fields. Warm colors show regions of positive vorticity whereas cool colors show areas of negative vorticity. (A–D) Vorticity plots for the porous model at *Re* 45 after (A) the second contraction, (B) the second full cycle, (C) the fourth contraction and (D) the fourth full cycle. (E–H) Corresponding plots at *Re* 450.

Equating the flux to the difference between the local fluid velocity and the boundary velocity results in an expression for the slip between the boundary and fluid that is proportional to the permeability and the pressure jump. This is incorporated into the immersed boundary method by modifying the velocity of the boundary. Rather than moving the boundary at the local fluid velocity, a slip is used that is proportional to the force per unit area acting normal to the boundary (which is proportional to the pressure jump) and the porosity. Eqn 10 is modified as follows:

$$\frac{\partial \mathbf{X}}{\partial t} = \mathbf{U}\left(s,t\right) + \lambda\left[\mathbf{F}\left(s,t\right) \bullet \mathbf{n}\right]\mathbf{n}\ , \qquad (14)$$

where λ is a proportionality constant termed the porosity by Kim and Peskin (Kim and Peskin, 2006) and **n** is the outward normal vector. Note that this has the effect of reducing the drag force applied to the fluid by the boundary. The physical interpretation of the porosity coefficient, λ, is that it is equal to the number of pores in an interval multiplied by the conductance of the material per unit arc length. The relationship between the porosity, λ, and the permeability, κ, is given by $\lambda=\kappa/(A\mu)$, where A is the area of the porous material. Kim and Peskin (Kim and Peskin, 2006) use the porosity coefficient in the slip term whereas Stockie (Stockie, 2009) uses the permeability, a value that can be readily found in the literature for a variety of materials. Estimates for the effective porosity or permeability of jellyfish oral arms are not known. For these simulations, several orders of magnitude of values for the porosity are considered. For the remaining simulations, a value is selected that produces flow profiles similar to what is observed experimentally. This value is chosen so that there is significant flow through the porous layer but the layer clearly alters the resulting flow patterns.

To model the oral arms in the simulations that follow, a line is defined of length L (the same length as the aboral region of the bell) as a reasonable approximation of length based on qualitative observations. The line is positioned just above the opening of the bell and is tethered in place using stiff Hookean springs that resist deformations in this part of the boundary. As a first approximation, the oral arm model is held in place and maintains a constant porosity. Physical parameters used for the simulations are given in Table 1.

Simulations were performed on a 512×512 periodic grid. The size of the domain was $4L\times4L$, where L is the length of the jellyfish bell. A box connected to tether points by stiff springs was added $L/8$ inside the edges of the domain to simulate the conditions in the laboratory tanks used for dPIV. The parameters used in the numerical simulation are given in Table 2. Times for the contraction, pauses and relaxation were taken from video footage as described previously. The mathematical model without the addition of the oral arms structure will be referred to as the base model. The models incorporating a porous membrane and an impermeable membrane will be referred to as the porous model and the impermeable model, respectively. *Re* was varied by changing the dynamic viscosity of the system. This method of changing *Re* has been used previously as an efficient means of exploring a large parameter space without having to vary multiple parameters (velocities and length scales) (Andersen et al., 2005; Wang, 2000).

RESULTS

Changes in *Re*

Vorticity plots with velocity vectors are shown for *Re*=45 and *Re*=450 in Fig. 3. Snapshots were taken during the second pulse cycle at the end of contraction (Fig. 3A,E) and at the end of expansion (Fig. 3B,F). Snapshots were also taken during the fourth cycle at the end of contraction (Fig. 3C,G) and at the end of expansion (Fig. 3D,H). The target boundary (purple) and the actual boundary (black) remain indistinguishable to the naked eye. Corresponding movies are given in supplementary material Movies 1 and 2. For *Re*=45, starting vortices form at the tip of the bell margin during the beginning of contraction, and oppositely signed stopping vortices form during the beginning of contraction. At the end of each phase,

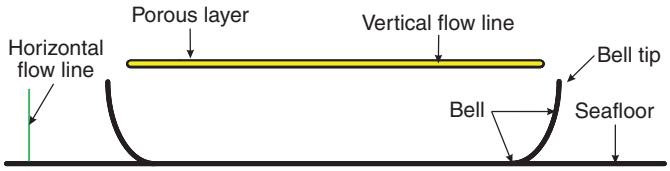

Fig. 4. The fully expanded model of the bell with the oral arms modeled as a porous layer. The substrate (floor) has been added to the model as a straight line one spatial gridpoint away from the model. The green line shows the positioning of the horizontal flow line (HFL) and the yellow line shows the position of the vertical flow line (VFL) where volume fluxes are calculated.

vorticity quickly dissipates, and the vortices do not appear to separate from the tip of the bell. For *Re*=450, starting and stopping vortices form at the beginning of contraction and expansion, respectively. In contrast to the low *Re* case the vortices do separate from the tips of the bell margins and are advected with the fluid along the porous layer. The fluid along the floor is pulled towards the bell on average during the cycle.

To quantify the bulk flow near and across the bell in the simulations, the volumetric flow rate (VFR) through a region was calculated. To calculate the VFR, a 'flow' line is drawn in a region so that the line is normal to the flow in the direction of interest. The instantaneous velocity in the normal direction is integrated along the flow line and is normalized against the length of the line to obtain the volume flux per unit length as:

$$\frac{V}{l} = \int_S \mathbf{u} \bullet \mathbf{n}\, \mathrm{d}S \,, \qquad (15)$$

where S is the flow line, $\mathbf{u}$ is the velocity along the line, $\mathbf{n}$ is the unit vector normal to the flow line, V is the volume flux and l is the length of the flow line. In this paper, two flow lines are defined. The first flow line is drawn vertically near the bottom of the tank to give a measurement horizontal flow toward the bell (Fig. 4). This flow line is referred to as the horizontal flow line (HFL), and its length is set equal to the height of the bell at a distance $L/4$ away from the outer edge of the relaxed bell. The second line, the vertical flow line (VFL), was drawn horizontally and overlaid on the center

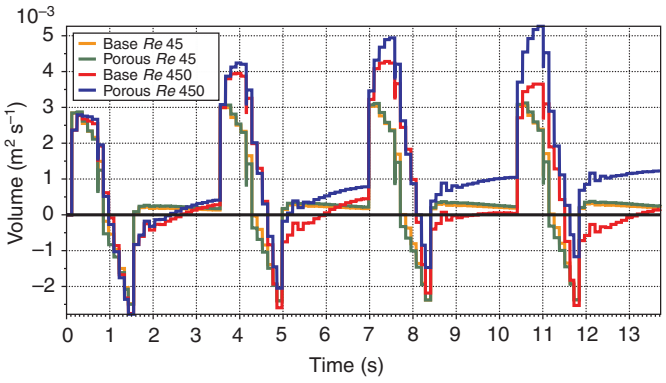

Fig. 5. Volumetric flow rates along the HFL describing horizontal flow moving towards the bell are compared among simulations of four different models. The base model at *Re* 45 is shown in orange, almost completely overlapped by the porous model (green). A base model (red) and a porous model (blue) at *Re*=450 are also shown. These plots indicate the normalized horizontal flow from the left of the domain toward the model organism. Positive flow indicates fluid moving towards the structure whereas negative flow indicates flow moving away from the structure.

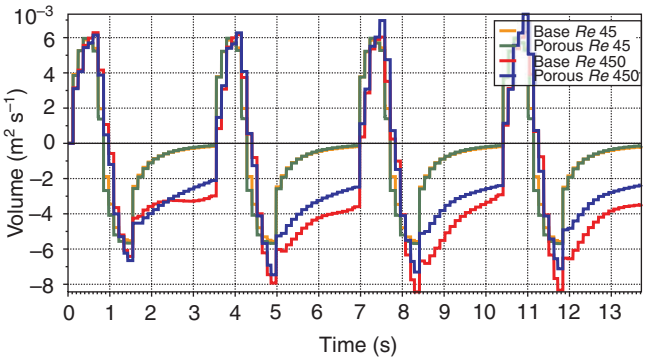

Fig. 6. Volumetric flow rates along the VFL describing vertical flow moving through the porous layer region are compared among simulations of four different models. The base model at *Re*=45 is shown in orange, almost completely overlapped by the porous model (green). A base model (red) and a porous model (blue) at *Re*=450 are also shown. These plots indicate the normalized vertical flow through the region where the porous structure (if present) is defined. Positive flow indicates fluid moving up and away from the structure whereas negative flow indicates flow moving down into the cavity of the structure.

of the porous structure. Its length was set to be L–$2\Delta s$, where Δs is the spatial step size on the Lagrangian grid, to ensure the flow line is in the region of the porous structure throughout the simulations. Typically Δs is set to one-half of the spatial step size on the Cartesian grid, Δx.

The VFRs at *Re*=45 and *Re*=450 along the HFL for models both with and without the porous structures are shown in Fig. 5 over four contraction cycles. Positive flow rates represent fluid motion towards the bell. For each simulation, the maximum VFR was attained during the contraction period of the cycle. During bell expansion, the VFR quickly decreased and became negative (flow moves away from the bell). After the end of the bell expansion, the VFR quickly approached zero. The minimum VFR (greatest flow rate away from the bell) decreased after each pulse in the *Re*=450 simulations with the added porous layer. In the other cases, significant amounts of backflow away from the bell during expansion persisted for all cycles. The VFR along the VFL is shown in Fig. 6. The maxima and minima of the flow rates occurred during the contraction and expansion, respectively. The magnitude of the VFL quickly dropped to zero for *Re*=45 when the jellyfish is at rest. For *Re*=450 a significant flow persisted through the porous layer during relaxation.

The effect of porosity

The effect of the oral arms on the flow was examined by comparing the base model with a model incorporating a permeable structure for the oral arms as well as with a model incorporating an impermeable structure. Representative vorticity plots with velocity vectors of the impermeable layer during the second and fourth cycles are shown in Fig. 7. Note that the way in which the starting and stopping vortices are advected in the fluid is altered depending upon the presence or absence of a layer. In the case of the porous layer in Fig. 3E–H, the vortices swirl around the outer edges of the simplified oral arms. For the case of the impermeable layer, a pair of oppositely spinning vortices is formed at each bell tip during the initial stages of contraction (in contrast to the formation of one starting vortex formed at each bell tip). This pair of vortices is quickly advected away from the bell. During expansion, another pair of oppositely signed vortices forms at each bell tip margin that

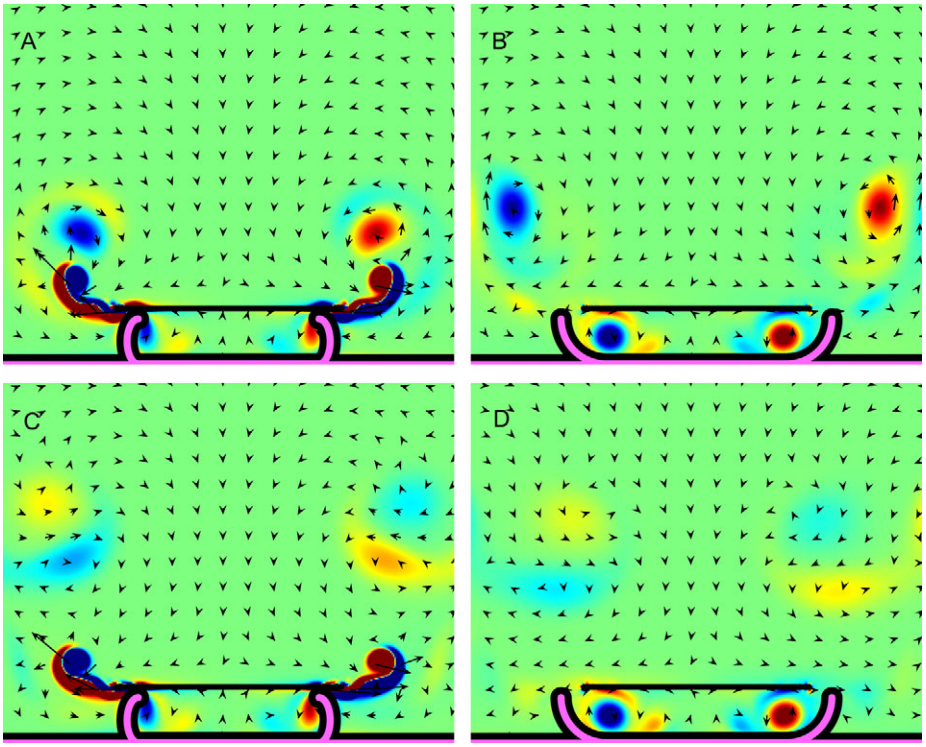

Fig. 7. Vorticity plots for the impermeable model from numerical simulations with overlaid velocity vectors. Warm colors show regions of positive vorticity whereas cool colors show areas of negative vorticity. (A–D) Vorticity plots for the impermeable model at *Re*=450 after (A) the second contraction, (B) the second full cycle, (C) the fourth contraction and (D) the fourth full cycle.

remains trapped between the bell and oral arms. In the absence of the oral arm layer (not shown in figures), starting and stopping vortices form during each cycle and swirl around the bell tips.

Plots of the VFRs along the HFL *vs* time for a porous layer model, an impermeable layer model and the base model at *Re*=450 are shown in Fig. 8. The maximum flow was achieved during contraction for the base model and the porous model whereas the maximum VFR for the impermeable model occurred during contraction in some pulses and during relaxation in others. The minimum VFR for the impermeable model decreased after each successive pulse cycle. The VFR along the VFL is shown in Fig. 9. The impermeable model shows much less flow than the porous and the base models, and the flow that is present is due to small deformations of the layer. The porous model and the base model show similar flow patterns throughout all four pulse cycles.

Values of the porosity coefficient λ that were 20 and 320% of the base case were compared for the porous model at *Re*=450 to determine how small changes in λ affected the flow around the jellyfish. Fig. 10 shows the VFR along the HFL. The VFR pattern is similar, but different in magnitude along the HFL throughout the pulse cycle. As the porosity of the porous layer increases, the maximum flow rate increases. As the porosity decreases, the flow rates approach the impermeable case as expected. The VFR along the VFL is shown in supplementary material Fig. S1. The pattern

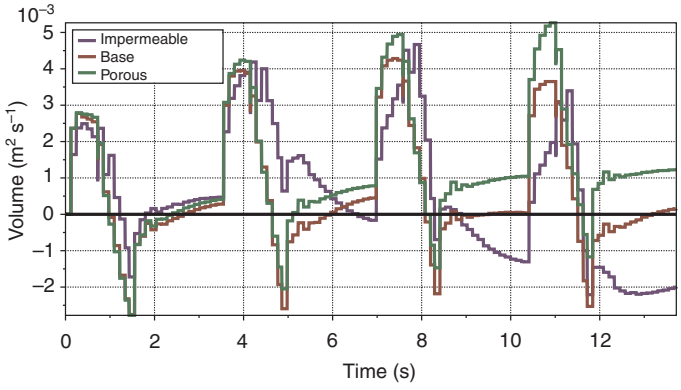

Fig. 8. Volumetric flow rates along the HFL describing horizontal flow moving towards the bell are compared among simulations of three different models. The base model at *Re*=450 is shown in purple. The porous model (green) and the impermeable model (red) are also shown at the same *Re*. These plots indicate the normalized horizontal flow from the left of the domain towards the model organism. Positive flow indicates fluid moving towards the structure whereas negative flow indicates flow moving away from the structure.

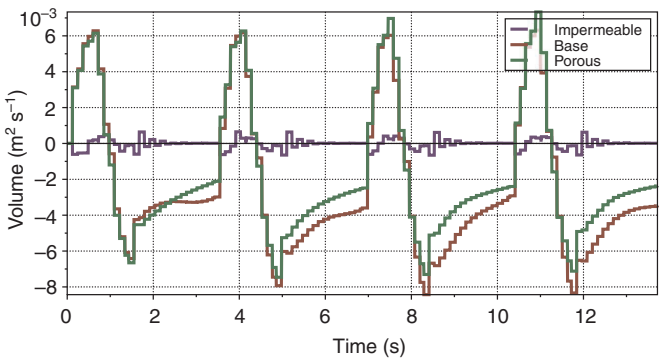

Fig. 9. Volumetric flow rates along the VFL describing vertical flow moving through the porous layer (if present) are compared among simulations of three different models. The base model at *Re*=450 is shown in purple. The porous model (green) and the impermeable model (red) are also shown at the same *Re*. These plots indicate the normalized vertical flow from through the region where the porous structure (if present) is defined. Positive flow indicates fluid moving up and away from the structure whereas negative flow indicates flow moving down into the cavity of the structure.

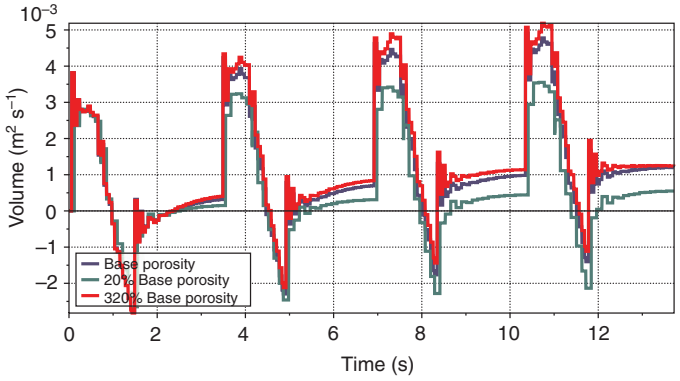

Fig. 10. Volumetric flow rates along the HFL describing horizontal flow moving towards the bell are compared among simulations of three different models. The porous model at *Re*=450 is shown in blue. Models with a porosity coefficient that is 20% of the porous model (green) and 320% of the porous model (red) are also shown at the same *Re*. These plots indicate the normalized horizontal flow from the left of the domain towards the model organism. Positive flow indicates fluid moving towards the structure whereas negative flow indicates flow moving away from the structure.

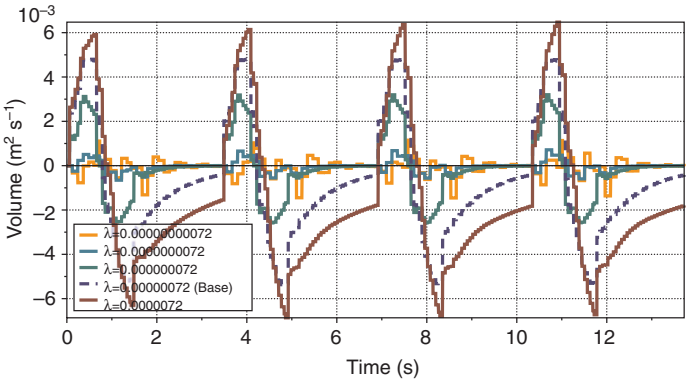

Fig. 11. Volumetric flow rates along the VFL describing vertical flow moving through the porous layer for values of the porosity, λ, ranging over four orders of magnitude. The dashed blue line denotes the value of the porosity chosen for the base cases. Note that when $\lambda=7.2\times10^{-10}$ the volumetric flow rate at the porous layer is similar to that of the solid layer. For values of λ between 7.2×10^{-7} and 7.2×10^{-6}, the volumetric flow rates at the layer are very similar.

of exchange is similar across the VFL for each value of the porosity with an increase in the maxima and minima similar to those across the HFL.

To test the choice of the porosity coefficient used in this in this paper, λ was varied over four orders of magnitude. Volumetric flow rates along the VFL describing vertical flow moving through the porous layers are shown in Fig. 11. The dashed blue line denotes the value of the porosity chosen for the base cases. Note that when $\lambda=7.2\times10^{-10}$ the volumetric flow rate at the porous layer is similar to the case of the solid layer. For values of λ between 7.2×10^{-7} and 7.2×10^{-6}, the difference in the volumetric flow rates are negligible despite the order of magnitude difference in λ. These results suggest that very small values of porosity will yield results similar to a solid layer whereas large values of porosity will have little effect on the flow. Intermediate values of λ alter the bulk flow while allowing some flow through the layer. The result is similar for a large range of intermediate λ.

The effect of the pauses

Vorticity plots with velocity vectors of the flow generated by a contracting and expanding bell without pauses are shown in Fig. 12. The vorticity during the second cycle is shown immediately after contraction (Fig. 12A) and immediately after expansion (Fig. 12B). The vorticity during the fourth cycle is also shown after contraction (Fig. 12C) and expansion (Fig. 12D). Continuous pulsing results in a train of vortices being advected vertically and away from the jellyfish. In comparison, when pauses are included (Fig. 3E–H) the vortices move around the porous layer and mostly dissipate before the next cycle.

Volumetric flow rates along the HFL were compared for a porous model with different pause times between complete expansion and the next contraction (Fig. 13). The maximum and minimum VFRs occurred during contraction and expansion, respectively. In general, the shorter the pause time the greater the magnitude and duration of backflow during expansion. A net flow towards the bell was also generated during relaxation; this decreased for pause times greater than 2 s.

Comparison of simulations with dPIV data

The vorticity plots from the simulation with porous arms in Fig. 3 were compared with data obtained using dPIV (A.S., M. Dollinger, C.H., S. P. Colin and L.A.M., submitted) (Fig. 14). dPIV is a non-intrusive experimental technique that can be used to obtain instantaneous information on a flow field by recording and processing the single or multiple exposed images of tracer particles

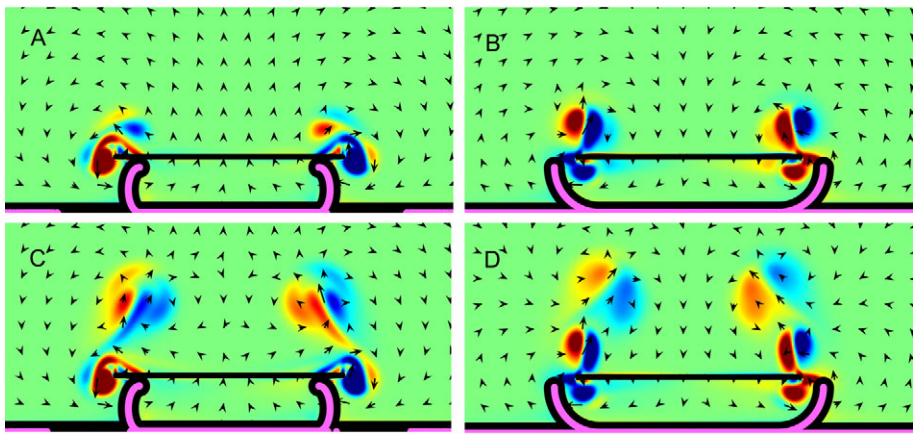

Fig. 12. Vorticity plots from numerical simulations with overlaid velocity vector fields for the porous model without a pause. Warm colors show regions of positive vorticity whereas cool colors are areas of negative vorticity. Vorticity fields are after (A) the second contraction, (B) the second full cycle, (C) the fourth contraction and (D) the fourth full cycle.

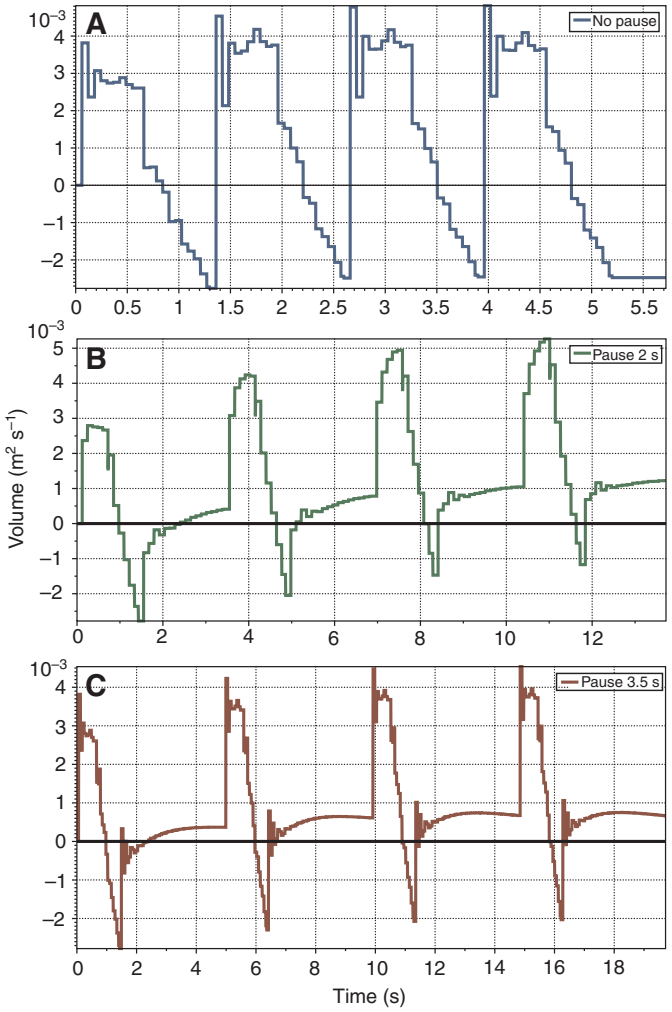

Fig. 13. Volumetric flow rates are compared among simulations of three different porous models. (A) A model with no pauses. (B) The standard porous model with a pause of 2 s between expansion and the following contraction. (C) A model with a pause of 3.5 s. These plots indicate the normalized horizontal flow from the left of the domain towards the model organism. Positive flow indicates fluid moving towards the structure whereas negative flow indicates flow moving away from the structure.

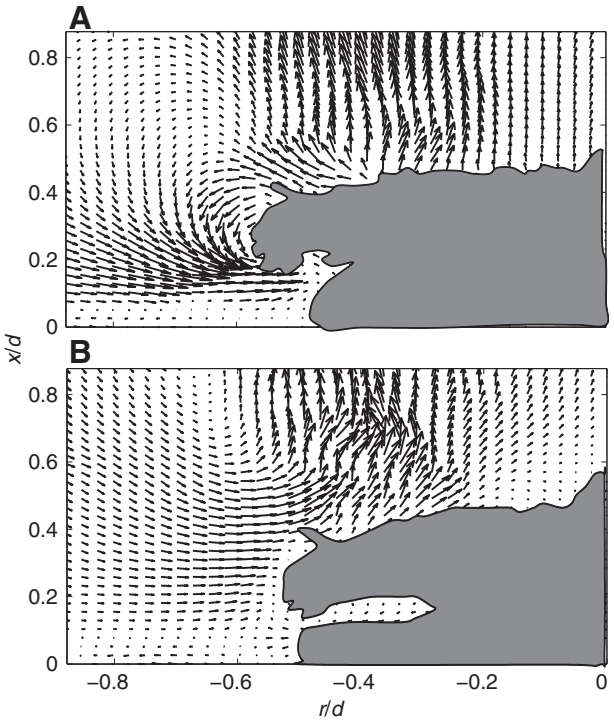

Fig. 14. Phase-locked velocity vector fields of the flow generated by *Cassiopea xamachana* of 6 cm maximum bell diameter using particle image velocimetry. The gray area is an overlaid image that shows the space filled by the organism. The results shown were obtained by averaging over 10 pulsing cycles, where the positions of the bell and oral arms were identical across all the individual realizations used in the averaging process. (A) The pulsing phase corresponding to full contraction of the bell; (B) the phase corresponding to full relaxation of the bell. *r*/*d*: radial distance over diameter; *x*/*d*, axial distance over diameter.

suspended in the fluid. The particle images are then processed using correlation-based techniques to construct the velocity vector field of the fluid flow (Adrian, 1991; Willert and Gharib, 1991). The dPIV images in Fig. 14 show the velocity vector fields generated by the pulse cycle of *C. xamachana* near the end of contraction (Fig. 14A) and near the end of expansion (Fig. 14B). Comparing Fig. 13A with Fig. 3G, the presence of a clear starting vortex can be seen at the end of contraction with strong flow moving along the floor towards the bell. Flow fields at the end of expansion (shown in Fig. 13B and Fig. 3H) show continued flow towards the bell, with the strongest flow upwards near the edge of the oral arms, as well as flow across the top of the oral arms. Neither the base nor the impermeable models exhibit similar flow structures. This indicates that both the presence of a porous obstruction (such as the oral arms) strongly influences the dynamics of the bulk fluid flow.

The velocity fields to the left of the bell in both the dPIV and the porous model show a constant flow towards the bell. Given the position of the HFL, a positive VFR indicates net flow toward the bell in that region whereas a negative value indicates flow away from the bell. From the dPIV data, constant flow toward the bell from the area near the floor is seen in the vector field plots. In Fig. 6, almost all of the flow along the substrate moves towards the bell after the third pulse. This is not the case in the base model or the impermeable model simulations (see Figs 6 and 8), and these results suggest that the presence of the oral arms play a role in driving the flow toward the bell.

DISCUSSION

The results presented here suggest that: (1) feeding from flows driven by bell contractions in a benthic organism may only be effective for *Re* on the order of 100 or higher, (2) the porous structure of the jellyfish oral arms can significantly alter bulk flow properties around the organism and (3) changes in the duration of the pause between bell contractions can significantly alter the resulting flow fields. Furthermore, the results suggest that the role of secondary structures such as the oral arms should be taken into account when designing models of some organisms, particularly oblate jellyfish with prominent feeding structures. In many oblate jellyfish, the oral arms comprise a significant portion of the body mass of the organism and often extend past the edges of the bell into the region of vortex formation (Bigelow, 1900; Hyman, 1940). Previous models of jellyfish have focused on how flow is driven to these structures, but the results here indicate that these structures may also alter the larger-scale flow field. The results support the hypothesis that jellyfish utilize bell pulsations not only for locomotion but also to actively

drive food particles to the secondary mouths. *Cassiopea* in particular rely on the ability to drive fluid for sampling, but other jellyfish that slowly cruise may be capitalizing upon this mechanism to compensate for the high cost of locomotion.

For *Re*=45, which is below the biologically relevant range of adult *C. xamachana*, little net flow is brought to the oral arms *via* the bell pulsations (see Fig. 7). A careful examination of the flow fields also indicates that little mixing occurs around the region of the oral arms. This suggests that there is a limit to the utility of pulsation as a particle transfer mechanism in the intermediate *Re* range. It is therefore not surprising that juvenile *Cassiopea* do not turn upside down and rest on the ocean floor until they reach a bell diameter of approximately 2 cm or more (Bigelow, 1900). Fig. 3 shows that at higher *Re* there is a larger amount of fluid exchanged back and forth across the oral arms, indicating that the pulsatile motion promotes water sampling in this range. Added together, the motion toward the bell and the increased sampling can be interpreted as enhancing the ability of the bell to bring in fresh materials from the substrate as well as the ability to sample the incoming fluid. The same sort of enhancement is not observed at lower *Re*.

Figs 7 and 9 indicate that the presence of an impermeable obstruction in the path of the flow not only prevents exchange across the secondary structure where feeding would occur but also directs flow from the substrate away from the bell, reducing the likelihood of particle sampling from the floor. This would indicate that a solid obstruction that inhibits flow through it would be less useful in enhancing feeding through pulsation. The flow pattern shown in Fig. 10 indicates that, without the secondary structure present, the fluid in the base model is moved back and forth as it moves towards the bell. This indicates that the porous layer plays an important role in bringing new fluid to the bell more quickly.

Laboratory observations show that *Cassiopea xamachana* exhibit different lengths of pauses between pulses (Hamlet et al., 2011). Fig. 12 shows the effect of adjusting the length of the pause between expansion and the subsequent contraction. From Fig. 12A it is seen that without a pause the flow does not move increasingly towards the bell with each cycle. This indicates a reduction in the amount of new fluid brought to the bell along the floor with each pulse. When the pause is introduced, the flow immediately above the oral arms moves across the layer with net flow at the oral arms moving downwards and potentially bringing food to the secondary mouths. Both kinds of cycles are observed in *Cassiopea xamachana*, and the results here indicate that slight modifications in the pulsing dynamics could significantly alter the resulting flow fields. For example, pauses might allow for the water that is brought into the bell to be sampled for a longer period of time. Pulsing cycles without pauses might be used for swimming and to move fluid up and away from the animal.

Limitations

A model that captures some of the fundamental qualitative patterns in the bulk flow across the bell of the upside-down jellyfish has been developed. Comparing this with PIV data it is shown that the flow field generated by the organism is similar in character to the results from numerical computations. Rather than trying to exactly match the morphology of the organism, important aspects of each structure have been represented by simple mathematical models that capture the fundamental nature of the mechanism. This simplification allows for larger parameter sweeps to explore the effects of morphology, scale and kinematics on bulk fluid flow. It is important to note, however, that these simplified models are not intended to replace detailed three-dimensional simulations that provide valuable insight into the physics of specific cases.

ACKNOWLEDGEMENTS

The authors thank Wanda Strychalski for her invaluable assistance with the numerical component of this work and David Adalsteinsson for assistance with DataTank software. We also thank Terry Campbell, William Kier, Tyson Hedrick, Peter Mucha and Gregory Forest for their advice and insights throughout this research project; and Terry Rodriguez, Megan Gyoerkoe and Makani Dollinger for their assistance with the live jellyfish. This work was partially funded by the Burroughs Wellcome Fund (BWF CASI ID #1005782.01) and by the National Science Foundation (NSF FRG #0854961, NSF DMS #1022802).

REFERENCES

Adrian, R. J. (1991). Particle imaging techniques for experimental fluid mechanics. *Annu. Rev. Fluid Mech.* **23**, 261-304.
Andersen, A., Pesavento, U. and Wang, Z. J. (2005). Analysis of transitions between fluttering, tumbling and steady descent of falling cards. *J. Fluid Mech.* **541**, 91-104.
Arai, M. N. (1996). *Functional Biology of Scyphozoa*. New York: Springer.
Bartleson, R. D. (2004). Interactions of seagrass beds and the water column: effects of bed size and hydrodynamics. PhD thesis, University of Maryland, College Park, MD, USA.
Beale, J. T. and Layton, A. T. (2009). A velocity decomposition approach for moving interfaces in viscous fluids. *J. Comput. Phys.* **228**, 3358-3367.
Bigelow, R. P. (1900). The anatomy and development of *Cassiopea xamachana*. *Boston Soc. Nat. Hist. Mem.* **5**, 191-236.
Brusca, R. C. and Brusca, G. J. (2003). *Invertebrates*. Sunderland, MA.: Sinauer Associates.
Colin, S. P. and Costello, J. H. (2003). *In situ* swimming and feeding behavior of eight co-occurring hydromedusae. *Mar. Ecol. Prog. Ser.* **253**, 305-309.
Dabiri, J. O. (2005). On the estimation of swimming and flying forces from wake measurements. *J. Exp. Biol.* **208**, 3519-3532.
Dabiri, J. O. (2008). Optimal vortex formation as a unifying principle in biological propulsion. *Annu. Rev. Fluid Mech.* **41**, 17-33.
Dabiri, J. O., Colin, S. P. and Costello, J. H. (2007). Morphological diversity of medusan lineages constrained by animal-fluid interactions. *J. Exp. Biol.* **210**, 1868-1873.
Dabiri, J. O., Colin, S. P. and Katija, K. (2010). A wake-based correlate of swimming performance and foraging behavior in seven co-occurring jellyfish species. *J. Exp. Biol.* **213**, 1217-1225.
Daniel, T. L. (1985). Cost of locomotion: unsteady medusan swimming. *J. Exp. Biol.* **119**, 149-164.
Daniel, T. L. (1995). Invertebrate swimming: integrating internal and external mechanics. *Symp. Soc. Exp. Biol.* **49**, 61-89.
Demont, M. E. and Gosline, J. M. (1988). Mechanics of jet propulsion in the hydromedusan jellyfish, *Polyorchis pexicillatus*: III. A natural resonating bell; the presence and importance of a resonant phenomenon in the locomotor structure. *J. Exp. Biol.* **134**, 347-361.
Dillon, R. H., Fauci, L. J. and Yang, X. (2006). Sperm motility and multiciliary beating: an integrative mechanical model. *Comput. Math. Appl.* **52**, 749-758.
Dillon, R. H., Fauci, L. J., Omoto, C. and Yang, X. (2007). Fluid dynamic models of flagellar and ciliary beating. *Ann. N. Y. Acad. Sci.* **1101**, 494-505.
Fauci, L. J. and Fogelson, A. L. (1993). Truncated Newton methods and the modeling of complex immersed elastic structures. *Commun. Pure Appl. Math.* **46**, 787-818.
Fauci, L. J. and McDonald, A. (1995). Sperm motility in the presence of boundaries. *Bull. Math. Biol.* **57**, 679-699.
Fauci, L. J. and Peskin, C. S. (1988). A computational model of aquatic animal locomotion. *J. Comput. Phys.* **77**, 85-108.
Fogelson, A. L. and Guy, R. D. (2008). Immersed-boundary-type models of intravascular platelet aggregation. *Comput. Methods Appl. Mech. Eng.* **197**, 2087-2104.
Hamlet, C., Miller, L. A., Rodriguez, T. and Santhanakrishnan, A. (2011). Fluid dynamics of feeding in the upside-down jellyfish. IMA (ed. S. Childress). In press.
Hou, T. Y. and Shi, Z. (2008). An efficient semi-implicit immersed boundary method for the Navier-Stokes equations. *J. Comput. Phys.* **227**, 8968-8969.
Hyman, L. H. (1940). *The Invertebrates: Protozoa through Ctenophora*. New York: McGraw-Hill.
Kim, Y. and Peskin, C. S. (2006). 2-D parachute simulation by the immersed boundary method. *SIAM J. Sci. Comput.* **28**, 2294-2312.
Kim, Y., Lai, M.-C. and Peskin, C. S. (2010). Numerical simulations of two-dimensional foam by the immersed boundary method. *J. Comput. Phys.* **229**, 5194-5207.
Lipinski, D. and Mohseni, K. (2009). Flow structures and fluid transport for the hydromedusae *Sarsia tubulosa* and *Aequora victoria*. *J. Exp. Biol.* **212**, 2436-2447.
Miller, L. A. and Peskin, C. S. (2009). Flexible clap and fling in tiny insect flight. *J. Exp. Biol.* **212**, 3076-3090.
Mittal, R. and Iaccarino, G. (2005). Immersed boundary methods. *Ann. Rev. Fluid Mech.* **37**, 239-261.
Peng, J. and Dabiri, J. O. (2008a). An overview of a Lagrangian method for analysis of animal wake dynamics. *J. Exp. Biol.* **211**, 280-287.
Peng, J. and Dabiri, J. O. (2008b). The 'upstream wake' of swimming and flying animals and its correlation with propulsive efficiency. *J. Exp. Biol.* **211**, 2669-2677.
Peng, J. and Dabiri, J. O. (2009). Transport of inertial particles by Lagrangian coherent structures: application to predator–prey interaction in jellyfish feeding. *J. Fluid Mech.* **623**, 75-84.

Peskin, C. S. (1977). Numerical analysis of blood flow in the heart. *J. Comput. Phys.* **25**, 220-252.
Peskin, C. S. (2002). The immersed boundary method. *Acta Numer.* **11**, 479-517.
Peskin, C. S. and McQueen, D. M. (1996). Fluid dynamics of the heart and its valves. In *Case Studies in Mathematical Modeling – Ecology, Physiology and Cell Biology* (ed. H. G. Othmer, F. R. Adler, M. A. Lewis and J. C. Dallon), pp. 309-337. Upper Saddle River, NJ: Prentice Hall.
Peskin, C. S. and Printz, B. F. (1993). Improved volume conservation in the computation of flows with immersed elastic boundaries. *J. Comput. Phys.* **105**, 33-46.
Rudolf, D. (2007). Animating jellyfish through numerical simulation and symmetry exploitation. MSc thesis, University of Saskatchewan, Saskatoon, SK, Canada.
Sahin, M., Mohseni, K. and Colin, S. P. (2009). The numerical comparison of flow patterns and propulsive performances for the hydromedusae *Sarsia tubulosa* and *Aequorea victoria*. *J. Exp. Biol.* **212**, 2656-2667.
Stockie, J. M. (2009). Modelling and simulation of porous immersed boundaries. *Comput. Struct.* **87**, 701-709.
Stockie, J. M. and Green, S. I. (1998). Simulating the motion of flexible pulp fibres using the immersed boundary method. *J. Comput. Phys.* **147**, 147-165.
Templeman, M. A. and Kingsford, M. J. (2010). Trace element accumulation in *Cassiopea* sp. (Scyphozoa) from urban marine environments in Australia. *Mar. Environ. Res.* **69**, 63-72.
Teran, J., Fauci, L. and Shelley, M. (2010). Viscoelastic fluid response can increase the speed and efficiency of a free swimmer. *Phys. Rev. Lett.* **104**, 038101.
Teran, J. M. and Peskin, C. S. (2009). Tether force constraints in stokes flow by the immersed boundary method on a periodic domain. *SIAM J. Sci. Comput.* **31**, 3404-3416.
Wang, Z. J. (2000). Vortex shedding and frequency selection in flapping flight. *J. Fluid Mech.* **410**, 323-341.
Watton, P. N., Luo, X. Y., Wang, X., Bernacca, G. M., Molloy, P. and Wheatley, D. J. (2007). Dynamic modelling of prosthetic chorded mitral valves using the immersed boundary method. *J. Biomech.* **40**, 613-626.
Welsh, D. T., Dunn, R. J. K. and Maeziane, T. (2009). Oxygen and nutrient dynamics of the upside down jellyfish (*Cassiopea* sp.) and its influence on benthic nutrient exchanges and primary production. *Hydrobiologia* **635**, 351-362.
West, E. J., Welsh, D. T. and Pitt, K. A. (2009). Influence of decomposing jellyfish on the sediment oxygen demand and nutrient dynamics. *Hydrobiologia* **616**, 151-160.
Willert, C. E. and Gharib, M. (1991). Digital particle image velocimetry. *Exp. Fluids* **10**, 181-193.
Wilson, M. M., Dabiri, J. O. and Eldredge, J. D. (2009). Lagrangian coherent structures in low Reynolds number swimming. *J. Phys. Condens. Matter* **21**, 204105.
Wolanski, E. (1992). Hydrodynamics of mangrove swamps and their coastal waters. *Hydrobiologia* **247**, 141-161.